Int. J. Electrochem. Sci., 15 **(2020)** 5632 – 5649, doi: 10.20964/2020.06.75

International Journal of
ELECTROCHEMICAL
SCIENCE
www.electrochemsci.org

Highly Porous Heteroatom Doped-Carbon Derived from Orange Peel as Electrode Materials for High-Performance Supercapacitors

Feifei Ding[1], Jin Li[1], Hongmei Du[1,2,], Jinsheng Zhao[1], Konggang Qu[1], Yunwu Li[1], Xianxi Zhang[1,*], Yan Zhang[1], Yao Qin[1] and Weiyu Lu[1]*

[1] School of Chemistry and Chemical Engineering, Liaocheng University, Shandong Provincial Key Laboratory of Chemical Energy Storage and Novel Cell Technology, Liaocheng 252059, China
[2] Key Laboratory of Advanced Energy Materials Chemistry (Ministry of Education), Nankai University, Tianjin 300071, China
[*]E-mail: duhongmei@lcu.edu.cn, zhangxianxi@lcu.edu.cn

Received: 2 February 2020 / *Accepted:* 31 March 2020 / *Published:* 10 May 2020

Biomass conversion to heteroatom-doped carbon materials is considered to be an effective and inexpensive method for energy conversion. Orange peel is rich in the elements carbon, nitrogen and oxygen. Herein, nitrogen and oxygen co-doped carbon is prepared by high-temperature carbonization and activation of orange peels. Two activating agents, KOH and K_2FeO_4, are adopted in the preparation. The OC-1-K sample derived from orange peel activated by KOH has a large specific surface area of 917.66 cm^2 g^{-1}. When used as a supecapacitor electrode material, the OC-1-K sample displays a high specific capacitance of 282.3 F g^{-1} at 1 A g^{-1}. Even when the current density increases to 20 A g^{-1}, the discharge capacity is 212 F g^{-1}, indicating good rate performance. After 4000 charge-discharge cycles in 2 mol L^{-1} KOH electrolyte, the capacitance is maintained at 209.8 F g^{-1} at 20 A g^{-1}, achieving good cycling stability. All these results are superior to those of the OC-1-G sample obtained by K_2FeO_4 activation. These results indicate that KOH is more effective in activating orange peels. The excellent electrochemical performance of the OC-1-K sample suggests good application prospects in supercapacitors.

Keywords: biomass-derived carbon, porous material, supercapacitive, symmetric supercapacitor

1. INTRODUCTION

Electrochemical energy storage systems, such as batteries and supercapacitors, have emerged as prospective energy storage systems for the rapid and environmentally friendly development of modern society [1]. Among these devices, supercapacitors are widely used in power-based fields due to their high power density, fast charging and discharging ability, long life and safety [1, 2]. However,

the energy densities of most existing supercapacitors are still limited, which has greatly impeded the large-scale applications of supercapacitors. Therefore, seeking materials with high energy densities is an urgent target for researchers [3, 4]. Carbon-based materials have attracted much attention bacause of their good chemical stability, high electrical conductivity, large surface area and controllable pore size [5, 6]. Unfortunately, some carbon materials are expensive, such as carbon nanotubes and graphene. Other carbon materials, such as carbon aerogels, require complex processes and toxic reagents for preparation. In addition, many of the reported activated carbon materials only possess a single microporous structure. The inner holes of these activated carbon materials are difficult to access by the electrolytes. Therefore, the reported activated carbon materials usually impart low capacitance and low energy density [6].

In recent years, renewable biomass-derived carbon materials have become popular candidates as supercapacitor materials [7-13]. Compared with traditional carbon materials, the direct use of biomass as a precursor to synthesize carbon materials can solve the problem of disposed wastes in terms of fruits, agricultural crops, and foods, among others. Therefore, such an approach is “green” for the environment and is easy to industrialize on a large scale. At the same time, when biomass is used to synthesize carbon materials, heteroatoms such as nitrogen and phosphorus are introduced in situ, which will have a beneficial role in the performance of the materials [14-16]. Orange is a widely grown plant, whose fruits are consumed almost all over the world. Orange peels are usually disposed, although some are used as medicinal herbs. It has been reported that orange peel contains approximately 50% cellulose, hemicellulose and lignin components based on the total dry mass. The high content of organic matter in the orange peel makes it difficult to dispose due to the high cost of homogenizing the different components [17]. However, this organic matter is a promising candidate to obtain carbon materials with high porosity and good electrical conductivity after carbonization, which is beneficial for ion transfer and electrolyte permeability and thus enhances the energy storage capacity [18].

The commonly used treatment method for biomass involves its activation by physical and chemical methods [19]. Physical activation involves the carbonization of the precursor. Chemical activation involves the reaction between the precursor and a chemical reagent, for example, KOH, K_2FeO_4 [2, 20-22], H_3PO_4 [23, 24], $ZnCl_2$ [7], H_2SO_4 and so on. The combination of physical and chemical activation of carbon materials can yield materials with large specific surface areas and highly porous structures [19]. Among the chemical activating agents, KOH and K_2FeO_4 have been widely used due to their effective role in activating carbon materials. However, a comparison of the same carbon precursor activated by these two different activating agents has not been reported.

Here, a two-step process for the preparation of nitrogen and oxygen co-doped carbon from orange peel by simultaneous carbonization and graphitization is proposed. Two activating agents, KOH and K_2FeO_4, are used separately in the preparation process. The OC-1-K sample obtained through KOH activation has a larger specific surface area (917.66 cm g^{-1}) than the OC-1-G sample obtained through K_2FeO_4 activation (438.62 cm g^{-1}). Benefiting from the larger accessible surface area and the appropriate pore size, the OC-1-K electrode shows a higher specific capacitance, excellent cycling performance and good rate capability. Furthermore, the assembled coin-type symmetric

supercapacitor shows a high energy density. This method opens an avenue for using biomass-derived materials to prepare carbon materials with excellent supercapacitive performance.

2. EXPERIMENTAL

2.1 Preparation of heteroatom-doped carbon from orange peel

Orange peels were first crushed and ultrasonically shaken with acetone and deionized water in order to remove impurities from their surfaces. After the orange peels were baked in an air-dry oven at 120 °C for 2 h, they were ground into powder. The obtained powder was placed in a tubular furnace and calcined at 550 °C for 2 h under a high-purity nitrogen atmosphere. The heating rate was 5 °C min^{-1}, and the obtained sample was denoted as OC-1.

OC-1 activated by KOH

Seven grams of KOH was dissolved in 50 mL of deionized water to form a transparent solution. Then, 6.0 g of OC-1 was immersed in the solution (the weight ratio of OC-1 to KOH was 3/3.5). After continuous stirring for 8 h, the material was placed in a vacuum drier at 60 °C for 10 h. The dried samples were placed in a tube furnace and calcined at 700 °C for 1 h under a nitrogen atmosphere. Then, they were washed with 1 mol L^{-1} hydrochloric acid, and neutralized to pH = 6-7 with distilled water. After vacuum drying, the obtained product was named OC-1-K.

OC-1 activated by K_2FeO_4

For comparison, OC-1 activated by K_2FeO_4 was produced by the same method as that with KOH activation. The sole difference was that KOH was changed to K_2FeO_4. The synthesized sample was labelled OC-1-G.

Formation mechanism of the OC-1-K and OC-1-G samples

The OC-1-K sample was prepared by the KOH activation of orange peel. The KOH activation process is a complicated process due to the variety in experimental parameters and the different reactivity of the precursors. The involved reactions can be summarized as follows:

$$2KOH \rightarrow K_2O + H_2O \quad (1)$$

$$C + H_2O \rightarrow CO + H_2 \quad (2)$$

$$CO + H_2O \rightarrow CO_2 + H_2 \quad (3)$$

$$CO_2 + K_2O \rightarrow K_2CO_3 \quad (4)$$

$$6KOH + 2C \rightarrow 2K + 3H_2 + 2K_2CO_3 \quad (5)$$

$$K_2CO_3 \rightarrow K_2O + CO_2 \quad (6)$$

$$CO_2 + C \rightarrow 2CO \quad (7)$$

$$K_2CO_3 + 2C \rightarrow 2K + 3CO \quad (8)$$

$$C + K_2O \rightarrow 2K + CO \quad (9)$$

To summarize, the KOH activation mechanism mainly involves three aspects: 1) chemical activation, which involve the etching of carbon materials by the redox reactions with different potassium species (eqn (5), (8) and (9)); 2) physical activation, which makes the products more porous through the gasification of carbon (eqn (2) and (7)); 3) the irreversible expansion of carbon lattices by the intercalation of K into the carbon matrix (eqn (5), (8) and (9)) [8].

The OC-1-G sample was prepared by the K_2FeO_4 activation of orange peel. K_2FeO_4 is used as both the activating agent (KOH) and catalyst (Fe species) to fulfill the synchronous carbonization and graphitization of orange peel (eqn (10). The amorphous Fe species ($Fe(OH)_3$, FeO(OH)) are progressively reduced to metallic Fe. Corresponding equations are listed below (eqn (11) to (13)) [2]. The metallic Fe acts as the catalyst in the graphitization process of amorphous carbon. [25].

$$4K_2FeO_4 + 10H_2O \rightarrow 8KOH + 4Fe(OH)_3 + 3O_2 \quad (10)$$

$$Fe(OH)_3 \rightarrow FeO(OH) \rightarrow Fe_2O_3 \quad (11)$$

$$3Fe_2O_3 + (H_2, C, CO) \rightarrow 2Fe_3O_4 + (H_2O, CO, CO_2) \quad (12)$$

$$Fe_3O_4 + 4(H_2, C, CO) \rightarrow 3Fe + 4(H_2O, CO, CO_2) \quad (13)$$

What should be pointed out is that, for the K_2FeO_4 activation process, all the reactions for the KOH activation and Fe species catalysis will take place, but the reactions do not necessarily take place as the orders shown above.

2.2 Characterization

The morphologies and microstructures of the samples were characterized by scanning electron microscopy (SEM, JEOL JSM-6700F) and transmission electron microscopy (TEM, JEM-2100, Japan). The composition and structure of the materials were investigated by X-ray powder diffraction (XRD, Bruker D8 Advance) with Cu Ka radiation. Nitrogen isotherms were recorded at -196 °C using a Micromeritics apparatus (ASAP 2460). Approximately 0.1 g of sample was first degassed under

vacuum at 200 °C for 2 h and then used for analysis. The specific surface areas were determined by the Brunauer-Emmett-Teller (BET) method within the appropriate relative pressure (P/P_0). The total pore volume was calculated based on the amount of nitrogen adsorbed at a relative pressure (P/P_0) of 0.995. Pore size distributions and micropore volumes were obtained through quenched-solid density functional theory (QSDFT). The valence states of the surface elements were determined using X-ray photoelectron spectroscopy (XPS, Thermo Scientific K Alpha). Raman spectra were detected on a confocal fluorescence Raman spectrometer (Monovista CRS500, 532 nm laser).

2.3 Electrochemical measurements

Galvanostatic charge-discharge (GCD), cyclic voltammetry (CV) and electrochemical impedance spectroscopy (EIS) tests were performed on an electrochemical workstation (Reference 3000, Gamry) using 2 mol L^{-1} KOH solution as the electrolyte. In a three-electrode configuration, nickel foam and a saturated calomel electrode (SCE) were used as the counter electrode and reference electrode, respectively. The working electrode was prepared through the slurry-coating method [26]. The as-prepared carbon, acetylene black and polyvinylidene fluoride (PVDF) were mixed at a weight ratio of 80:15:5. Then, 3-4 drops of N-methylpyrrolidone were added into the mixture. The mixture was ground to a homogeneous slurry and applied it to the foamed nickel (1 cm×1 cm). The coated nickel foam was vacuum-dried at 60 °C for 12 h. The foam was placed between two nickel foams (3 cm × 3 cm) and compressed by a tableting machine to form the working electrode. The applied weight of the active material in the working electrode was approximately 4.3 mg. CV tests were conducted between -1.0 and 0 V (vs. SCE) with scan rates ranging from 5 to 100 mV s^{-1}. The different current densities adopted in the GCD tests were chosen as 1.0, 2.0, 5.0, 10.0 and 20.0 A g^{-1}. EIS was conducted at an open-circuit potential with an amplitude of 5 mV. The operating frequency range was 0.01 to 10^5 Hz.

The two-electrode symmetric supercapacitor was assembled using two identical OC-1-K electrodes sandwiched between cellulose paper (used as the separator) with 2 mol L^{-1} KOH solution as the electrolyte. The method for preparing the working electrode was the same as that in the three-electrode system. CV and GCD tests were performed between 0 and 1 V. The EIS parameters were the same as those in the three-electrode system.

3. RESULTS AND DISCUSSION

3.1 Morphological and structural characterization

The morphology and microstructure of the OC-1-K sample were characterized by SEM and TEM. As displayed in the SEM images in Fig. 1a-b, the OC-1-K sample has initial pore structures on the smooth surface, and the pores are irregular, which are formed through the KOH activation process and high temperature carbonization under N_2. Many mesopores and micropores are observed in the TEM images. Abundant voids are favourable for electrolyte penetration and provide more electroactive chemical sites during electrochemical reaction processes.

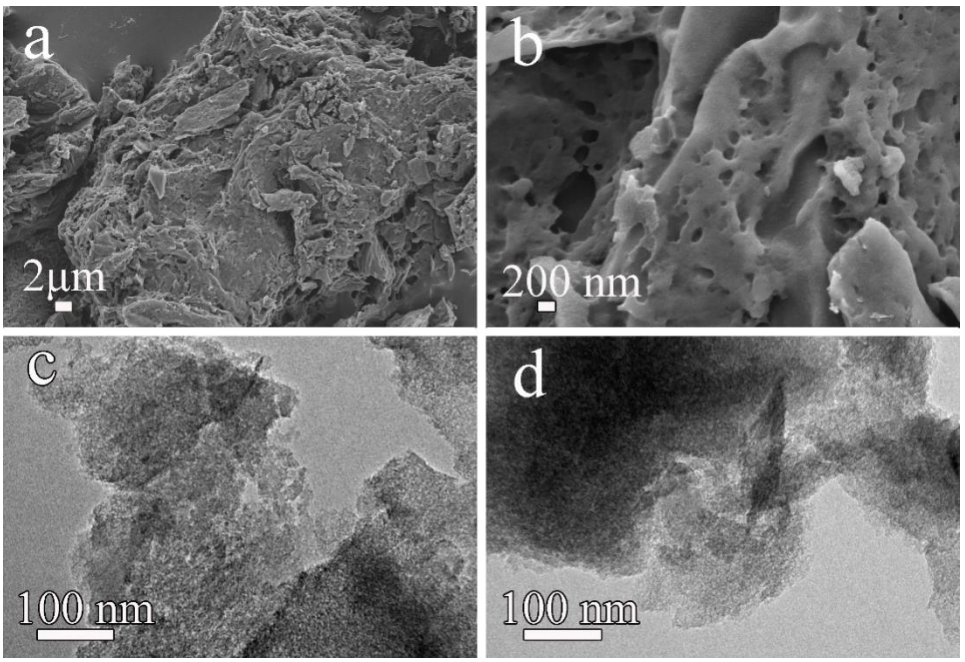

Figure 1. SEM and TEM images of the OC-1-K sample: (**a, b**) SEM images; (**c, d**) TEM images

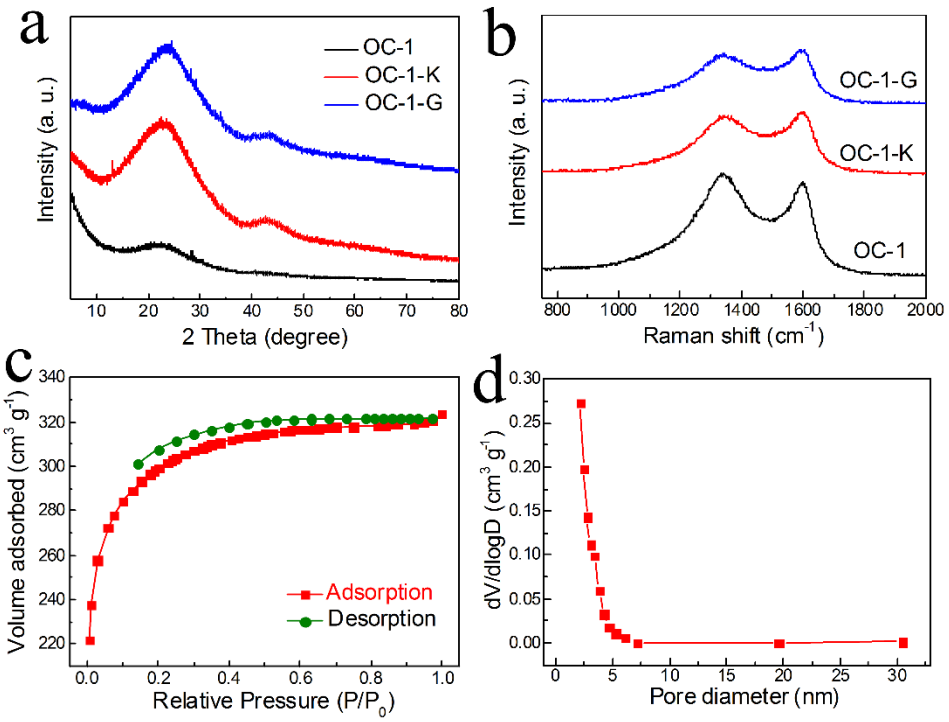

Figure 2. (**a**) XRD patterns and (**b**) Raman spectra using 532 nm excitation of OC-1, OC-1-K and OC-1-G; (**c**) N_2 adsorption-desorption isotherm of the OC-1-K sample; (**d**) pore size distribution of the OC-1-K sample

The composition and graphitization degree of the three samples were investigated by XRD and Raman spectroscopy. The XRD patterns of the OC-1-K and OC-1-G samples shown in Fig. 2a both display two diffraction peaks at 2θ values of 21.8 and 43.6°, which belong to the typical (002) and (101) reflections of graphitic carbon, respectively [27]. For comparison, OC-1 displays only one broad

peak, indicating its amorphous carbon structure. It is obvious that the graphitization degrees of the OC-1-K and OC-1-G samples increase after high temperature calcination. A higher graphitization degree often relates to a higher electrical conductivity, which is favourable for charge transfer and directly improves the electrochemical performance [28]. The (002) peak of OC-1-K is slightly broader than that of OC-1-G, indicating the more unordered nature of the sample [29]. The large intensity increases in the low-angle regions of the OC-1 and OC-1-K samples indicate the presence of large amounts of micropores [30]. The Raman spectra of the OC-1, OC-1-K and OC-1-G samples displayed in Fig. 2b exhibit two bands at ~ 1350 cm^{-1} and 1580 cm^{-1}. The D band at ~ 1350 cm^{-1} relates to the defect sites of graphite or disordered sp^2-hybridized carbon atoms. The G band at ~ 1580 cm^{-1} is attributed to the in-plane vibrations of sp^2 carbon atoms. The degree of crystallinity or defect density of carbon materials is usually determined by the intensity ratio of the D band to the G band (I_D/I_G). The I_D/I_G values of the OC-1, OC-1-K and OC-1-G samples are 1.08, 0.86 and 0.84, respectively. The I_D/I_G value for the OC-1-K sample is lower than that of OC-1 but higher than that of OC-1-K, indicating the enhanced degree of disorder and defects caused by KOH activation compared to the sample activated by K_2FeO_4 [29, 31].

The nitrogen adsorption-desorption curves and pore size distribution of the OC-1-K sample are displayed in Fig. 2c-2d. The corresponding results of the OC-1 and OC-1-G samples are shown in Fig. S2. The major N_2 adsorption for the OC-1-K sample occurs in the low relative pressure region (P/P_0=0.2), and the desorption curves are almost horizontal in the high relative pressure region, indicating that the OC-1-K sample possesses high microporosity [28, 32]. The hysteresis loop between the absorption and desorption isotherms indicates the presence of mesopores [33]. The hysteresis loop area in the N_2 sorption isotherm is smaller in the OC-1-K and OC-1-G samples than in the OC-1 sample, indicating a more accessible porous structure [33]. The BET surface areas and pore structures of the OC-1, OC-1-K and OC-1-G samples are summarized in detail in Table 1. The OC-1-K sample displays the maximal BET surface area (917.66 m^2 g^{-1}) and largest pore volume. There is an increase in the V_{micro}/V_{total} (the volume ratio of micorpores to total pores) values among the OC-1, OC-1-K and OC-1-G samples (0.78, 0.68 and 0.62, respectively), indicating an increase in mesopore volume, which is consistent with the XRD results. It is possible that some of the micropores are changed to mesopores during the KOH/K_2FeO_4 activation and carbonization process. Large surface areas are beneficial for the penetration of electrolyte during electrochemical operation, thus enhancing the specific capacitance and rate capability. The hierarchical multi-pore structure combined with micropores, mesopores and macropores is effective for the transport of ions and shortens the diffusion pathways during electrochemical processes. According to previous reports, pores with sizes between 0.4 and 1 nm are favourable for the desolvation of ions and are thus able to contribute to capacitance at low current densities [34, 35]. The meso- and macropores can serve as buffering reservoirs and shorten the distance travelled by the electrolyte, which can guarantee the supply of electrolyte during electrochemical processes [36].

Table 1. BET specific surface areas and pore structures of the samples

Samples	BET surface area (m^2g^{-1})	Total pore volume (cm^3g^{-1})	Micropore volume (cm^3g^{-1})
OC-1	160.51	0.0950	0.0741
OC-1-K	917.66	0.5001	0.3393
OC-1-G	438.62	0.2616	0.1610

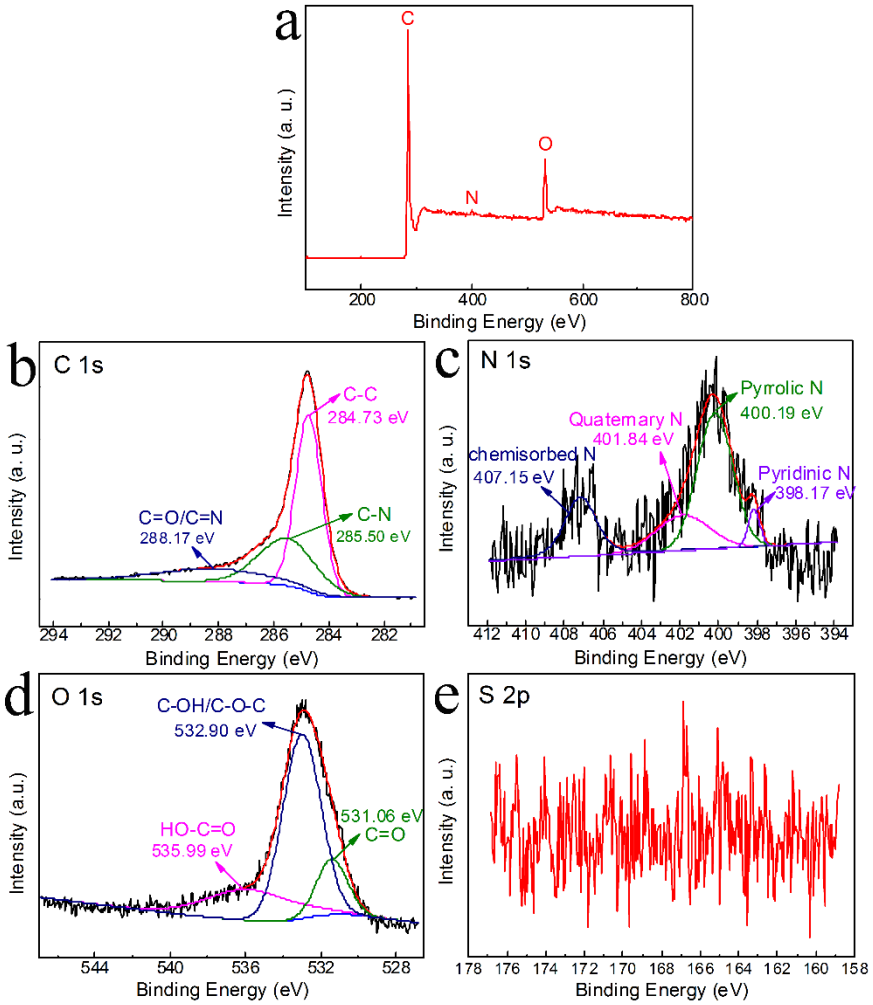

Figure 3. XPS spectra of the OC-1-K sample: (**a**) survey; (**b**) C 1s; (**c**) N 1s; (**d**) O 1s; (**e**) S 2p

The elemental compositions and valence states of the surface elements were investigated by XPS. As shown in Fig. 3a, the sample contains C, N, O, and S, and no other impurity elements are detected. The atomic percentages of C, N, O and S in the OC-1-K sample are 86.39%, 3.12%, 10.36% and 0.13%, respectively. According to the fitting results shown in Fig. 3b, the C 1s spectrum is deconvoluted into three peaks centred at 284.73, 285.5 and 288.17 eV, which are assigned to graphite

(C-C), C-N and C=O/C=N, respectively [2, 37], further suggesting the successful doping of nitrogen into the atomic skeleton of carbon and ample O-rich functional groups [38]. The N 1s spectrum is fitted into four peaks at 398.17, 400.19, 401.84 and 407.15 eV, corresponding to pyridinic-N (4.62%), pyrrolic-N (51.75%), quaternary-N (20.12%) and chemisorbed nitrogen species (23.51%), respectively [39]. The O 1s spectrum contains many functional groups such as quinone-type C=O groups at 531.06 eV [14], C-OH phenol groups and/or C-O-C ether groups at 532.90 eV and chemisorbed oxygen (COOH, carboxylic groups) and/or water at 535.99 eV [33, 40, 41]. Possibly due to the low atomic ratio of S in the sample, it is not detected in the survey spectrum. For comparison, the XPS investigation for the OC-1-G sample was also performed, and the results are displayed in Fig. S1. The atomic percentages of C, N, O and S in the OC-1-G sample are 88.13%, 3.31%, 8.51% and 0.16%, respectively.

3.2 Electrochemical performance of the OC-1-K electrode

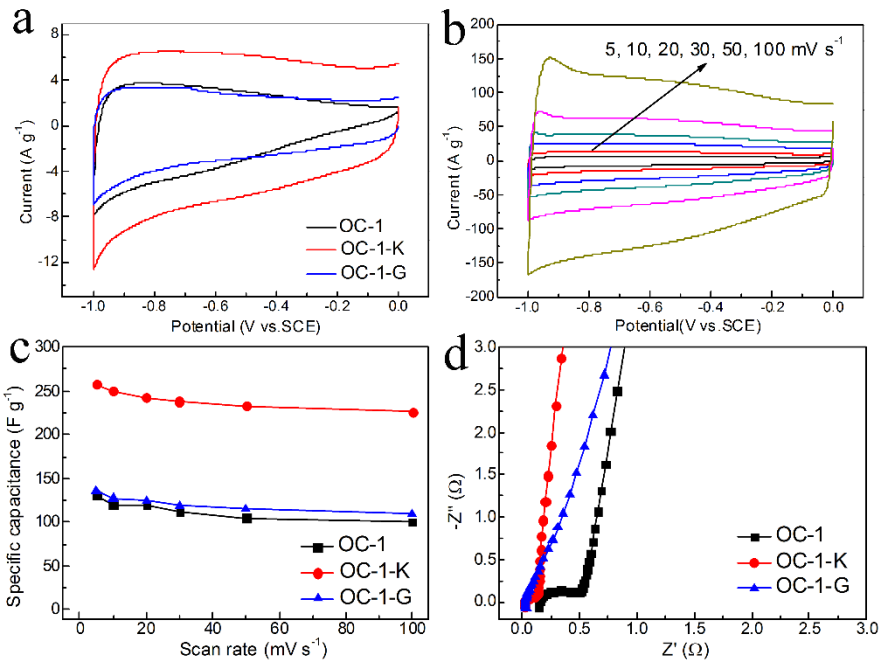

Figure 4. (**a**) CV plots of different samples at a scan rate of 5 mV s^{-1}; (**b**) CV curves at different scan rates of the OC-1-K sample; (**c**) Specific capacitance comparison of the three electrodes at a scan rate of 5mV s^{-1} .(**d**) EIS spectrum of the three samples. All the tests were performed in 2.0 mol L^{-1} KOH electrolyte.

The supercapacitive performance of the three samples was first evaluated in a three-electrode system through CV, GCD and EIS measurements. The corresponding results are presented in Fig. 4 and Fig. 5. As displayed in Fig. 4a, compared to the CV curves of the OC-1 and OC-1-G electrodes, the CV profile of the OC-1-K electrode displays a more quasi-rectangular shape, revealing the typical electrochemical double-layer capacitance (EDLC) nature originating from the reversible ion adsorption/desorption process. The tiny deformation from the rectangular shape may result from the

limited pseudocapacitance originating from the N,O-doped functional groups, as confirmed by the XPS results shown in Fig. 3 [2, 27]. The specific capacitance is determined through eqn (14):

$$C = \frac{\int_{V_1}^{V_2} i(V)d(V)}{vm(V_2 - V_1)} \quad (14)$$

where i(V) is the instantaneous current, V_1 and V_2 are the lower and upper potentials in the CV tests, i(V)dV is the total charge obtained from the CV curves, m is the weight of the active material, and v is the scan rate.

Based on eqn (1), the specific capacitances of the three samples at 5 mV s^{-1} are 250 F g^{-1} for OC-1-K, 100.1 F g^{-1} for OC-1 and 135.7 F g^{-1} for OC-1-G (Fig. 5a), indicating that the sample activated by KOH exhibits the best supercapacitive performance. The CV curves of OC-1-K measured at different scan rates are recorded in Fig. 4b. As the scan rate increases, the CV curve of the OC-1-K sample maintains a good rectangular shape, indicating good capacitive behaviour and efficient charge transfer [41]. For comparison, the CV curves of the OC-1 electrode are distorted at high scan rates (shown in Fig. S3), indicating its poorer supercapacitive performance, which may be ascribed to the smaller surface area and lower conductivity. The specific capacitances of the three samples at different scan rates are summarized in Fig. 4c. Obviously, the specific capacitances of the samples decrease gradually as the scan rate increases. The reason for this trend is that at a higher scan rate, there is insufficient time for ion diffusion and electron transfer, so the reaction does not proceed sufficiently. Specifically, the OC-1-K sample shows the maximum specific capacitance and best rate capability.

To further explore the advantages of the OC-1-K electrode, we obtained EIS spectra of OC-1-K, OC-1 and OC-1-G, and the results are displayed in Fig. 4d. The semicircle in the high-frequency region represents the charge transfer resistance in the electrochemical processes. The intersection with the real axis at high frequency involves the intrinsic electronic properties between the electrode matrix and the electrolyte. The quasi-vertical line at a low frequency indicates dominant double-layer charge storage and excellent supercapacitive performance. The inclined line close to the theoretical vertical line for the OC-1-K electrode indicates the excellent pore accessibility of the electrolyte [42]. The slight deviation from the ideal 90° slope towards the real axis is partly derived from the pseudocapacitance provided by heteroatom doping [43]. Based on the results shown in Fig. 4d, the OC-1-K electrode displays smaller charge transfer resistance and Warburg resistance than the OC-1-G and OC-1 electrodes, indicating its better faradaic charge transfer properties and capacitive behaviour.

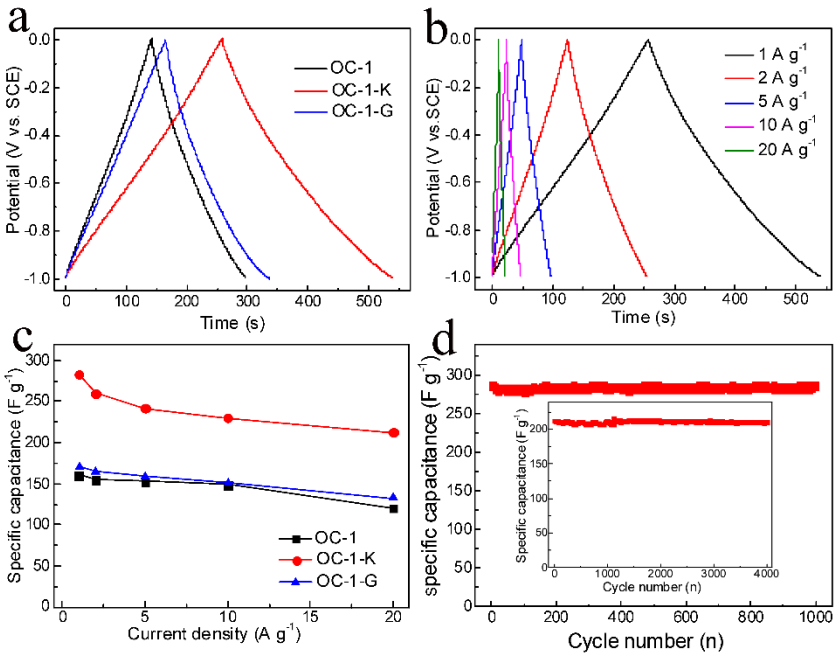

Figure 5. (**a**) GCD curves of the OC-1, OC-1-K and OC-1-G electrodes at a current density of 1A g^{-1}; (**b**) GCD curves of the OC-1-K electrode at different current densities (1, 2, 5, 10 and 20 A g^{-1}); (**c**) Specific capacitance comparison of the three electrodes at different current densities; (**d**) Specific capacitance versus the cycle number for the OC-1-K electrode at a current density of 1.0 A g^{-1}, Inset shows the cycling performance of the OC-1-K electrode at a current density of 20.0 A g^{-1}

The GCD curves of the OC-1, OC-1-K and OC-1-G electrodes at a current density of 1 A g^{-1} are displayed in Fig. 5a. The linear nature of the charge and discharge curves proves the electrical double-layer capacitive performance. The small deviation is caused by heteroatom doping, which is consistent with the CV results. The specific capacitance is calculated by eqn (15):

$$C = \frac{I\Delta t}{m\Delta V} \quad (15)$$

where C (F g^{-1}) designates the specific capacitance, I (A) represents the discharge current density (A g^{-1}), Δt (s) is the discharge time, m (g) is the mass of active materials and ΔV (V) is the potential drop during the discharge process.

It is obvious that the specific capacitance of the OC-1-K sample is higher than that of the OC-1 and OC-1-G samples, in accordance with the CV results. The GCD curves for the OC-1-K electrode at different current densities are displayed in Fig. 5b. The quasi-linear nature of the GCD curves validates the graphitization and improved conductivity [43]. At a high current density of 20 A g^{-1}, the charge-discharge curve is still smooth and displays a symmetrical isosceles triangle shape, which further proves its good rate performance. The specific capacitances of the OC-1-K electrode at current densities of 1, 2, 5, 10 and 20 A g^{-1} are 282.3, 260.4, 242, 230 and 212 F g^{-1}, respectively. These values have surpassed those of many of the previously reported biomass-based carbon materials (Table 2). For comparison, the specific capacitances of the OC-1-G electrode at current densities of 1, 2, 5, 10 and 20 A g^{-1} are 170.0, 164.6, 158.3, 150.6 and 132.6 F g^{-1}, respectively, only slightly higher than those of the

OC-1 electrode. The OC-1-K sample also shows good cycling stability. As shown in Fig. 5d, the specific capacitance after 1000 cycles is still stable at 260 F g^{-1}, which is 94% of the initial capacitance. The inset in Fig. 5d shows the cycling curve of the OC-1-K electrode at a current density of 20 A g^{-1}. Even after 4000 cycles, the specific capacitance still remains at 209.8 F g^{-1}, indicating its excellent cycling stability.

Table 2. Comparison of the properties of carbon materials synthesized from biomass resources and their use in supercapacitors.

Biomass precursor	Activation method	SSA[1] (m^2 g^{-1})	C[2] (F g^{-1})	Current density or scan rate	Electrolyte	Reference
Orange peel	$FeCl_3$	1514.2	255	0.5 A g^{-1}	6 mol L^{-1} KOH	[18]
Corn grains	KOH	3199	257	1 mA cm^{-2}	6 mol L^{-1} KOH	[44]
Ginkgo shells	KOH	1775	178	500 mV s^{-1}	6 mol L^{-1} KOH	[45]
Seaweed biopolymer	Thermal	273	198 in the two electrode system	2 mV s^{-1}	1 mol L^{-1} H_2SO_4	[46]
Carbon/ZnO	Hydrothermal	818.9	117.4	0.5 A g^{-1}	6 mol L^{-1} KOH	[47]
Wood sawdust	KOH	2294	225	0.5 A g^{-1}	6 mol L^{-1} KOH	[48]
sago bark	pyrolysis	58	113 in the two electrode system	20 mA g^{-1}	5 mol L^{-1} KOH	[49]
animal bone	pyrolysis	2157	185 in the two electrode system	0.05 A g^{-1}	7 mol L^{-1} KOH	[50]
Fungi	Hydrothermal pyrolyis	80.08	196	5 mV s^{-1}	6 mol L^{-1} KOH	[51]
waste paper	KOH	416	180	2 mV s^{-1}	6 mol L^{-1} KOH	[52]
Human hair	Hydrothermal KOH	849	264	0.5 A g^{-1}	6 mol L^{-1} KOH	[53]

The high specific capacitance and good cycling stability of the OC-1-K sample can be ascribed to the following reasons. First, nitrogen and oxygen functional groups can increase the wettability of

[1] BET specific surface area
[2] Gravimetric capacitance in the three electrode system

carbon materials and provide additional pseudocapacitance [43]. Typically, pyrrolic-N and phenol type-O can both contribute to pseudocapacitance in alkaline solutions [54]. As shown in Table S1, the atomic ratios of pyrrolic-N and phenol type-O in the OC-1-K sample are apparently higher than those in the OC-1-G sample. Second, the better ion and electron transport capacity of the OC-1-K sample compared to OC-1-G is proven by the EIS result in Fig. 4d. In addition, quaternary-N is beneficial to increasing the conductivity of the material, which contributes to the cycling stability of the supercapacitor [41]. Third, a compromise between the higher graphitization degree and the higher disorder degree of the OC-1-K sample endows it with the best supercapacitive performance. Last but not least, the synergetic effect between the high electrochemical conductivity and large surface area contributes to the better supercapacitive performance. The higher proportion of micropores, as well as the presence of some mesopores in the OC-1-K sample makes it possible to take full advantage of the electrolytes.

3.3 Electrochemical performance of a symmetric supercapacitor

To further investigate the practical application of the OC-1-K electrode, a symmetric supercapacitor was assembled using two identical OC-1-K electrodes separated by a cellulose separator. The electrolyte was a 2 mol L^{-1} KOH solution. The CV curves of the symmetric supercapacitor shown in Fig. 6a exhibit quasi-rectangular shapes without apparent distortion even at a high scan rate of 100 mV s^{-1}, indicating good rate capability. The GCD curves presented in Fig. 6b show almost linear symmetrical triangular shapes, indicating good electrochemical performance. There are no obvious IR drops in the GCD curves for the symmetric supercapacitors shown in Fig. 6b. The specific capacitances of the symmetric device are obtained from the GCD curves through eqn (16) [54]:

$$C_{cell} = \frac{I\Delta t}{m\Delta V} \tag{16}$$

where C_{cell} (F g^{-1}) is the specific capacitance of the symmetric device, Δt (s) is the discharge time, m (g) is the total mass of the two electrodes, and ΔV (V) is the voltage window.

Specifically, the specific capacitance of the symmetric device at 1 A g^{-1} is 37.7 F g^{-1}. This value decreases accordingly with increasing current density. For example, the specific capacitances at 1.5 and 2 A g^{-1} are 34.1 F g^{-1} and 33.4 F g^{-1}, respectively. The reduced capacitance at high current density is due to the inefficient contact between the electrolyte and the active materials. However, the supercapacitor retains almost 100% of its initial capacitance after 2000 cycles at 1.0 A g^{-1}, indicating good cyclic stability.

The energy density and power density of the symmetric device are further calculated according to eqns (17) and (18). Detailed data are summarized in the Ragone plots shown in Fig. 6d.

$$E = \frac{C_{cell}\Delta V^2}{7.2} \tag{17}$$

$$p = \frac{3600E}{\Delta t} \tag{18}$$

where E (Wh kg^{-1}) is the energy density, C_{cell} (F g^{-1}) is the specific capacity of the symmetric device, ΔV (V) is the cell voltage, P (W kg^{-1}) is the power density and Δt (s) is the discharge time.

The maximum energy density of the symmetric supercapacitor is 5.24 Wh kg^{-1} at a power density of 500 W kg^{-1}. The energy density remains at 4.64 Wh kg^{-1} at a higher power density of 1000 W kg^{-1}.

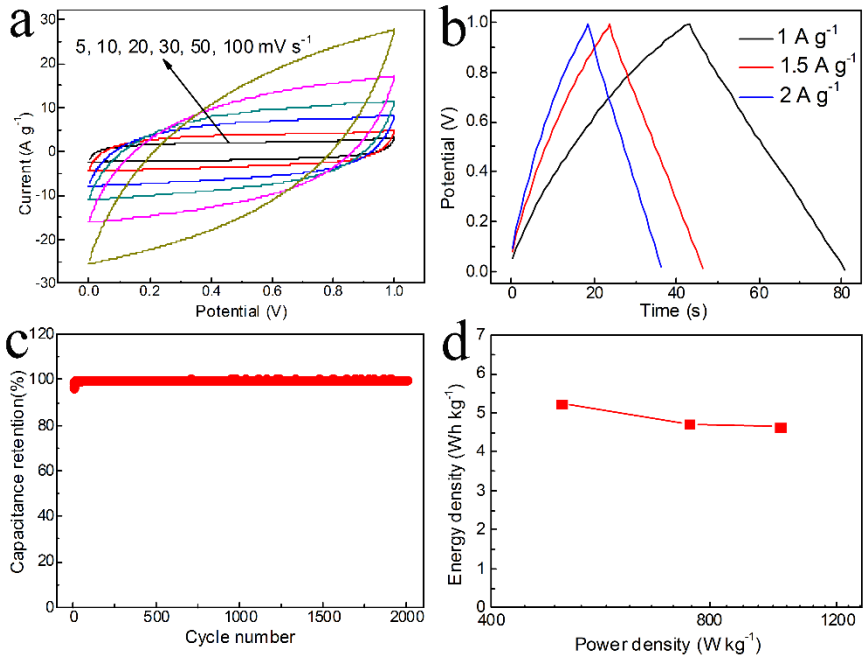

Figure 6. (**a**) CV plots of the symmetric supercapacitor at different scan rates in a 2.0 mol L^{-1} KOH electrolyte. (**b**) GCD images at different current densities; (**c**) Capacitance retention curve of the symmetric supercapacitor; (**d**) Ragone plots

4. CONCLUSIONS

In summary, porous carbonaceous nanoparticles are obtained through high-temperature carbonization and activation of orange peel. Two kinds of activating agents, KOH and K_2FeO_4, are adopted in the preparation processes. The experimental results indicate that the OC-1-K sample obtained through the KOH activation process imparts a larger BET surface area, larger pore volume and higher conductivity. The OC-1-K sample shows a large BET surface area of 917.66 m^2 g^{-1}. When used in a supercapacitor, the OC-1-K electrode displays a higher specific capacitance and better rate capability than the OC-1-G electrode obtained through K_2FeO_4 activation. The OC-1-K electrode shows a maximum capacitance of 283 F g^{-1} at 1 A g^{-1}. It maintains approximately 99% of its original capacitance after 4000 cycles at 20 A g^{-1}, indicating excellent cycling stability and rate capacity. In addition, the two-electrode symmetric supercapacitor exhibits excellent cycling stability and high energy density. We expect this synthetic method to broaden our horizons in synthesizing high-performance carbon materials from renewable biomass.

ACKNOWLEDGMENTS
This work was supported by the National Natural Science Foundation of China [21601079, 51473074, 21771095] and the Shandong Provincial Natural Science Foundation [ZR2017JL013, ZR2019MEM031]. The author also thanks the financial support from development project of Youth Innovation Team in Shandong Colleges and universities (2019KJC031) and Colleges and universities in Shandong Province science and technology projects (Grant No. J17KA097).

References

1. A. Noori, M.F. El-Kady, M.S. Rahmanifar, R.B. Kaner, M.F. Mousavi, *Chem. Soc. Rev.*, 48 (2019) 1272.
2. Y. Gong, D. Li, C. Luo, Q. Fu, C. Pan, *Green Chem.*, 19 (2017) 4132.
3. W. Raza, F. Ali, N. Raza, Y. Luo, K.-H. Kim, J. Yang, S. Kumar, A. Mehmood, E.E. Kwon, *Nano Energy,* 52 (2018) 441.
4. A. González, E. Goikolea, J.A. Barrena, R. Mysyk, *Renew. Sust. Energ. Rev.*, 58 (2016) 1189.
5. T. Liu, F. Zhang, Y. Song, Y. Li, *J. Mater. Chem. A,* 5 (2017) 17705.
6. A. Borenstein, O. Hanna, R. Attias, S. Luski, T. Brousse, D. Aurbach, *J. Mater. Chem. A,* 5 (2017) 12653.
7. L. Sun, C. Tian, M. Li, X. Meng, L. Wang, R. Wang, J. Yin, H. Fu, *J. Mater. Chem. A,* 1 (2013) 6462.
8. J. Wang, S. Kaskel, *J. Mater. Chem.*, 22 (2012) 23710.
9. W.-J. Liu, H. Jiang, H.-Q. Yu, *Chem. Rev.,* 115 (2015) 12251.
10. S. Dutta, A. Bhaumik, K.C.W. Wu, *Energy Environ. Sci.*, 7 (2014) 3574.
11. Y.-P. Gao, Z.-B. Zhai, K.-J. Huang, Y.-Y. Zhang, *New J. Chem.*, 41 (2017) 11456.
12. Z. Wang, D. Shen, C. Wu, S. Gu, *Green Chem.*, 20 (2018) 5031.
13. S. Zhou, L. Zhou, Y. Zhang, J. Sun, J. Wen, Y. Yuan, *J. Mater. Chem. A,* 7 (2019) 4217.
14. J. Ou, Y. Zhang, L. Chen, Q. Zhao, Y. Meng, Y. Guo, D. Xiao, *J. Mater. Chem. A,* 3 (2015) 6534.
15. K. Qu, Y. Zheng, S. Dai, S.Z. Qiao, *Nano Energy,* 19 (2016) 373.
16. K. Qu, Y. Zheng, Y. Jiao, X. Zhang, S. Dai, S.-Z. Qiao, *Adv. Energy Mater.,* 7 (2017) 1602068.
17. K. Xiao, H. Liu, Y. Li, L. Yi, X. Zhang, H. Hu, H. Yao, *Bioresour. Technol.,* 265 (2018) 432.
18. H. Gou, J. He, G. Zhao, L. Zhang, C. Yang, H. Rao, *Ionics,* 25 (2019) 4371.
19. W. Gu, G. Yushin, *Wiley Interdisciplinary Reviews-Energy and Environment,* 3 (2014) 424.
20. L. Hou, Z. Hu, X. Wang, L. Qiang, Y. Zhou, L. Lv, S. Li, *J. Colloid Interface Sci.,* 540 (2019) 88.
21. J. Zhou, Y. Guo, C. Liang, J. Yang, J. Wang, Y. Nuli, *Electrochim. Acta,* 273 (2018) 127.
22. P. Zhang, X. Tan, S. Liu, Y. Liu, G. Zeng, S. Ye, Z. Yin, X. Hu, N. Liu, *Chem. Eng. J.,* 378 (2019) 122141.
23. C. Huang, T. Sun, D. Hulicova-Jurcakova, *ChemSusChem,* 6 (2013) 2330.
24. Q. Wei, Z. Chen, Y. Cheng, X. Wang, X. Yang, Z. Wang, *Colloids Surf., A: Physicochemical and Engineering Aspects,* 574 (2019) 221.
25. F.J. Maldonado-Hódar, C. Moreno-Castilla, J. Rivera-Utrilla, Y. Hanzawa, Y. Yamada, *Langmuir,* 16 (2000) 4367.
26. H. Du, Y. Li, F. Ding, J. Zhao, X. Zhang, Y. Li, R. Zhao, M. Cao, T. Yu, X. Xu, *Int. J. Hydrogen Energy,* 43 (2018) 15348.
27. J. Deng, T. Xiong, F. Xu, M. Li, C. Han, Y. Gong, H. Wang, Y. Wang, *Green Chem.*, 17 (2015) 4053.
28. J. Li, Y. Gao, K. Han, J. Qi, M. Li, Z. Teng, *Sci Rep,* 9 (2019) 17270.
29. W. Qian, J. Zhu, Y. Zhang, X. Wu, F. Yan, *Small,* 11 (2015) 4959.
30. Y.Y. Soo, C.S. Youn, S. Jinyong, K.B. Hoon, C. Sung-Jin, B.S. Jae, H.Y. Suk, T. Yongsug, P.Y. Woo,

P. Sungjin, J. Hyoung-Joon, *Adv. Mater.*, 25 (2013) 1993.
31. M. Li, C. Liu, H. Cao, H. Zhao, Y. Zhang, Z. Fan, *J. Mater. Chem. A,* 2 (2014) 14844.
32. Q. Wang, Q. Cao, X. Wang, B. Jing, H. Kuang, L. Zhou, *J. Power Sources*, 225 (2013) 101.
33. X. Li, B.Y. Guan, S. Gao, X.W. Lou, *Energy Environ. Sci.*, 12 (2019) 648.
34. J. Chmiola, C. Largeot, P.-L. Taberna, P. Simon, Y. Gogotsi, *Angew. Chem. Int. Ed.*,47 (2008) 3392.
35. J. Chmiola, G. Yushin, Y. Gogotsi, C. Portet, P. Simon, P.L. Taberna, *Science*, 313 (2006) 1760.
36. P. Hao, Z. Zhao, J. Tian, H. Li, Y. Sang, G. Yu, H. Cai, H. Liu, C.P. Wong, A. Umar, *Nanoscale*, 6 (2014) 12120.
37. Q. Lu, J. Yu, X. Zou, K. Liao, P. Tan, W. Zhou, M. Ni, Z. Shao, *Adv. Funct. Mater.*, (2019) 1904481.
38. R. Liu, H. Zhang, S. Liu, X. Zhang, T. Wu, X. Ge, Y. Zang, H. Zhao, G. Wang, *Phys. Chem. Chem. Phys.*, 18 (2016) 4095.
39. C. Tang, B. Wang, H.-F. Wang, Q. Zhang, *Adv. Mater.*, 29 (2017) 1703185.
40. Y.-Q. Zhao, M. Lu, P.-Y. Tao, Y.-J. Zhang, X.-T. Gong, Z. Yang, G.-Q. Zhang, H.-L. Li, *J. Power Sources*, 307 (2016) 391.
41. X. Wei, Y. Li, S. Gao, *J. Mater. Chem. A*, 5 (2017) 181.
42. M.D. Stoller, R.S. Ruoff, *Energy Environ. Sci.*, 3 (2010) 1294.
43. H. Zhu, X. Wang, X. Liu, X. Yang, *Adv. Mater.*, 24 (2012) 6524.
44. M.S. Balathanigaimani, W.-G. Shim, M.-J. Lee, C. Kim, J.-W. Lee, H. Moon, *Electrochem. Commun.*, 10 (2008) 868.
45. L. Jiang, J. Yan, L. Hao, R. Xue, G. Sun, B. Yi, *Carbon*, 56 (2013) 146.
46. E. Raymundo-Piñero, F. Leroux, F. Béguin, *Adv. Mater.*, 18 (2006) 1877.
47. Y. Li, X. Liu, *Mater. Chem. Phys.*, 148 (2014) 380.
48. Y. Huang, L. Peng, Y. Liu, G. Zhao, J.Y. Chen, G. Yu, *ACS Appl. Mater. Interfaces*, 8 (2016) 15205.
49. G. Hegde, S.A. Abdul Manaf, A. Kumar, G.A.M. Ali, K.F. Chong, Z. Ngaini, K.V. Sharma, *ACS Sustainable Chem. Eng.*, 3 (2015) 2247.
50. W. Huang, H. Zhang, Y. Huang, W. Wang, S. Wei, *Carbon*, 49 (2011) 838.
51. H. Zhu, X. Wang, F. Yang, X. Yang, *Adv. Mater.*, 23 (2011) 2745.
52. D. Kalpana, S.H. Cho, S.B. Lee, Y.S. Lee, R. Misra, N.G. Renganathan, *J. Power Sources*, 190 (2009) 587.
53. W. Si, J. Zhou, S. Zhang, S. Li, W. Xing, S. Zhuo, *Electrochim. Acta*, 107 (2013) 397.
54. R. Zhang, X. Jing, Y. Chu, L. Wang, W. Kang, D. Wei, H. Li, S. Xiong, *J. Mater. Chem. A*, 6 (2018) 17730.

SUPPORTING INFORMATION

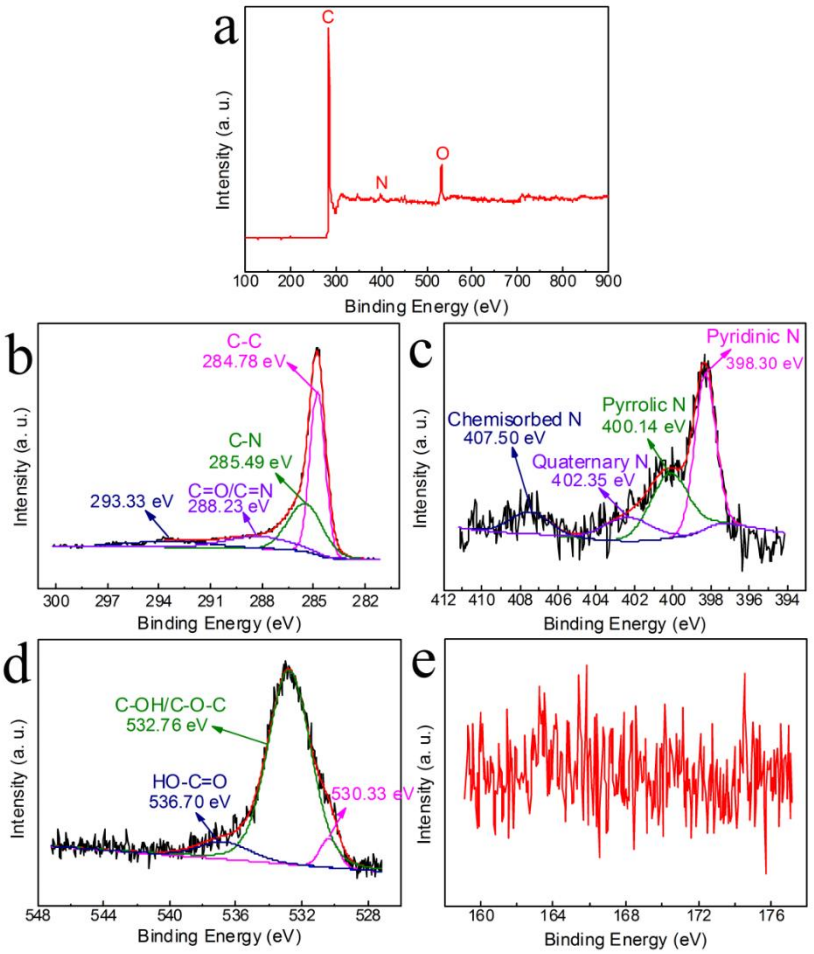

Fig. S1 XPS spectra of the OC-1-G sample: (**a**) survey; (**b**) C 1s; (**c**) N 1s; (**d**) O 1s; (**e**) S 2p

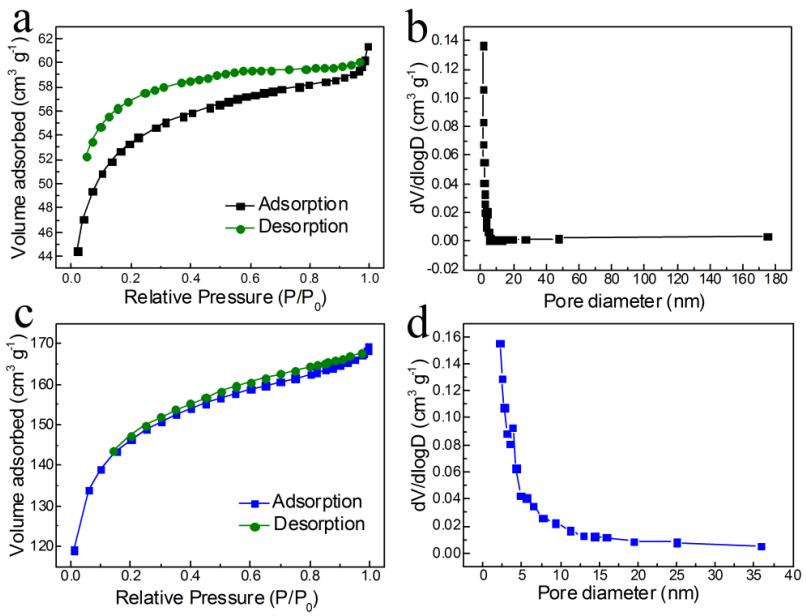

Fig. S2 N_2 adsorption-desorption isotherm of the (**a**) OC-1 and (**c**) OC-1-G samples; pore size distribution of the (**b**) OC-1 and (**d**) OC-1-G samples

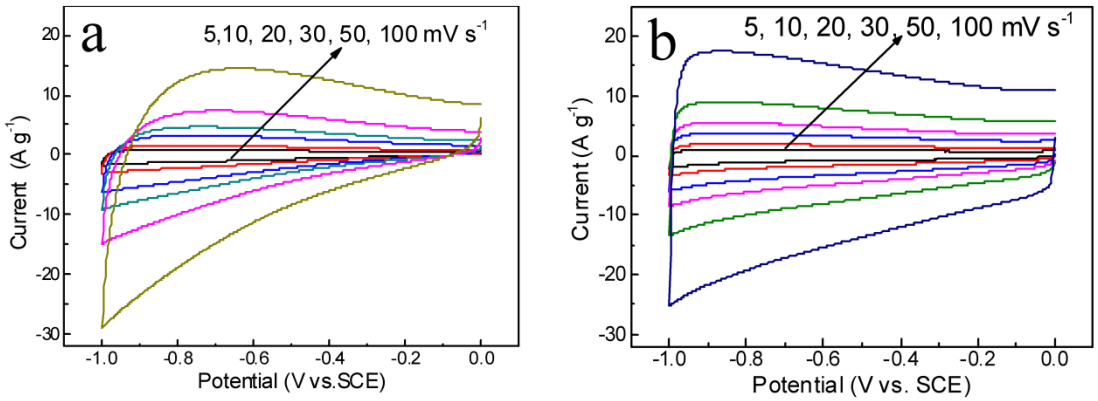

Fig. S3 CV curves at different scan rates of the sample (**a**); without activation; (**b**) activated by K_2FeO_4

Table S1. Relative atomic contents of nitrogen and oxygen species obtained by fitting N1s and O1s XPS spectra

sample	Nitrogen species (%)				Oxygen species (%)			Active species
	Pyridinic N	Pyrrolic N	Quaternary N	Chemisorbed N	Quinone-type O	Phenol-type O	Ether-type O	Pyrrolic N+ Phenol-type O
OC-1-K	0.17	1.78	0.50	0.66	0.89	7.29	2.18	9.07
OC-1-G	1.35	1.03	0.46	0.36	0.44	7.27	0.79	8.30